

# Disentangling heterogeneity and disorder during ultrafast surface melting of orbital order

Maurizio Monti<sup>1,2\*</sup>, Khalid M. Siddiqui<sup>1\*</sup>, Daniel Perez-Salinas<sup>1,3</sup>, Naman Agarwal<sup>1</sup>, Martin Bremholm<sup>4</sup>, Xiang Li (李翔)<sup>5</sup>, Dharmalingam Prabhakaran<sup>6</sup>, Xin Liu<sup>7</sup>, Danylo Babich<sup>7</sup>, Mathias Sander<sup>7</sup>, Yunpei Deng<sup>7</sup>, Henrik T. Lemke<sup>7</sup>, Roman Mankowsky<sup>7</sup>, Xuerong Liu (柳学榕)<sup>5,8†</sup>, Simon E. Wall<sup>1#</sup>

1. *Department of Physics and Astronomy, Aarhus University, Aarhus, Denmark*
2. *Institut des Molécules et Matériaux du Mans, UMR CNRS 6283, Le Mans Université, 72085 Le Mans, France*
3. *ALBA Synchrotron Light Source, Barcelona, Spain*
4. *Department of Chemistry, Aarhus University, Aarhus, Denmark*
5. *School of Physical Science and Technology, ShanghaiTech University, Shanghai 201210, China*
6. *Department of Physics, Clarendon Laboratory, University of Oxford, Oxford, OX1 3PU, UK*
7. *Swiss Light Source, Paul Scherrer Institut, Villigen, Switzerland*
8. *Center for Transformative Science, ShanghaiTech University, Shanghai 201210, China*

*\*Equal contribution*

<sup>†</sup> [liuxr@shanghaitech.edu.cn](mailto:liuxr@shanghaitech.edu.cn)

<sup>#</sup> [simon.wall@phys.au.dk](mailto:simon.wall@phys.au.dk)

**Understanding how light modifies long-range order is key to improve our ability to control material functionality on an ultrafast timescale. Transient spatial heterogeneity has been proposed in many materials, but isolating the dynamics of different regions experimentally has been challenging. Here we address this issue and measure the dynamics of orbital order melting in the layered manganite,  $\text{La}_{0.5}\text{Sr}_{1.5}\text{MnO}_4$ , and isolate the surface dynamics from the bulk for the first time. Bulk measurements show orbital order is rapidly suppressed, but the correlation length surprisingly increases. However, the surface dynamics, show a stronger suppression and a significant decrease in correlation length. By isolating the surface changes, we find that light preferentially melts a less ordered surface and the loss of long-range order is likely driven by the formation of local and disordered polarons. Melting the disordered surface effectively increases the average correlation of the bulk probed volume, resolving the contradictory response. These results show that surface scattering methods are necessary to understand both surface and bulk dynamics in heterogeneous materials.**

Rapid developments of novel laser spectroscopies, X-ray lasers and ultrafast electron sources are providing more and more details on how materials transform, and multiple scenarios have emerged. Some materials show a homogeneous transition, in which the amplitude of the order is suppressed without generating defects in contrast to thermal transitions<sup>1,2</sup>, while others shown a heterogeneous response. Light has been able to induce transient non-equilibrium phases on the nanoscale<sup>3,4</sup> and changed the ratio between two competing, but pre-existing phases<sup>5,6</sup>. Yet the reason why some materials show a

heterogeneous response in the time domain, and others are not well understood, which limits our ability to control materials.

Implicit in the understanding of measurements to date is that the dynamics come from the bulk, and the possible contribution of the surface has been ignored. The latter presumption is problematic as the surface is often a source of heterogeneity. This is particularly true of phase transitions, where the different environment at the surface can cause phase transitions to occur at different temperatures and length scales than their bulk counterparts<sup>7-10</sup>. In addition, the controlling laser penetrates only 100s of nanometres into the bulk and thus most ultrafast dynamics are occurring in this near-surface region.

Advances in ultrafast X-ray<sup>11</sup> and near-field<sup>12</sup> imaging now enable measurements of in-plane heterogeneity down to the nanoscale on the ultrafast timescale and time-resolved LEED can measure changes in the surface structure<sup>13</sup>, but observing out-of-plane heterogeneity, from the surface and into the bulk, has not been demonstrated. To overcome this limitation, we use ultrafast X-ray surface scattering<sup>14</sup> to get access to the dynamics that occur exclusively at the crystal surface of a bulk crystal for the first time and compare our results to those obtained from the bulk order measured through a Bragg peak within the same experiment for the first time. Such time-resolved surface scattering techniques have only become possible due to high brightness XFEL sources. We find that the surface response is in stark contrast to the bulk order and furthermore, that understanding the surface response is key to correctly interpreting the bulk response.

In this paper, we study the photo-response of orbital order in the single-layered manganite  $\text{La}_{0.5}\text{Sr}_{1.5}\text{MnO}_4$ . In equilibrium, orbital order phase transition is heterogeneous and is strongly influenced by the surface<sup>9,10</sup>. But while the role of heterogeneity has been considered in the long-term recovery of order in these materials<sup>15</sup>, its role on the ultrafast timescale has received less attention. Both optical<sup>16,17</sup> and X-ray<sup>18-20</sup> measurements have been interpreted assuming that the material response is homogenous. This has led to the suggestion that the phase transition is a coherent and ordered phenomenon driven by a single order parameter and global potential energy surface. However, more recent optical measurements have suggested that coherence does not play a role in the phase transition and surface heterogeneity needs to be taken into account when interpreting the data<sup>21</sup>. Therefore, we re-examine the melting process and the role played by the surface.

**Figure 1a** shows the experimental setup used to achieve surface sensitivity. Experiments were performed at the SwissFEL instrument Bernina. Surface sensitivity with X-rays can be achieved by measuring the  $(-0.25, 2.25, L)$  orbital truncation rod (OTR) in the vicinity of  $L=0$ , which is scattering that arises from the orbital surface in the material. Scattering from this region is maximized in a grazing incidence. To probe the bulk order, we measure the  $(-0.25, 2.25, 2)$  orbital Bragg peak (OBP). To preserve pump and probe penetration depths, we keep the same grazing incidence angle for both measurements. The sample was cooled to 180 K, to be in the orbitally ordered phase which has a critical temperature of approximately  $T_c = 220$  K (see methods for details).

We start by discussing the response of the OBP, which is the quantity traditionally used to understand the material dynamics. Analysis of the peak width before excitation gave an in-plane correlation length of  $\zeta_{ab} = 250 \text{ \AA}$ , and out of plane correlation of  $\zeta_c = 81 \text{ \AA}$ , in good agreement with previous measurements<sup>9,10</sup>. **Fig. 1b** show the temporal evolution of a cut through the OBP along the L direction (see the inset of Fig.1b). Upon excitation with 800 nm pump, the peak intensity reduces as the amplitude of

the orbital order is rapidly suppressed within the experimental time resolution and then remains constant. However, surprisingly, the width of the remaining peak narrows on the same timescale, suggesting the residual order has a longer correlation length. The narrowing also occurs in the in-plane direction as found from a full three-dimensional scan of the pumped OBP shown in **extended data figure 1**.

If we assume the sample was homogenous before excitation, i.e. the correlation length is independent of depth from the surface as has been done in analysis to date<sup>18–20</sup>, the observed photo-induced narrowing of 10% would mean that the surviving regions of orbital order must *increase* their correlation length. Such a photo-induced annealing processes, while exotic, has been proposed to explain width changes in materials with competing charge density wave order<sup>6</sup>. However, if the material starts in a heterogeneous state, alternative interpretations are possible. We note that we could only suppress the OBP intensity by ~30% with a pump fluence as high as 12 mJ/cm<sup>2</sup>. At these fluences, optical measurements suggest the order should be completely melted<sup>21</sup>. This suggests we are probing a larger volume than that which is excited despite the fact that optical and X-ray penetration depths should be well matched (see methods). Therefore, observing what is happening at the surface is key for interpreting the bulk data.

**Figure 2** summarises the results of the surface scattering measurements. **Figure 2a** shows cuts through the OTR before excitation which reveals an in-plane correlation length,  $\zeta_s \sim 40 \text{ \AA}$  (see methods), consistent with previous measurements<sup>9,10</sup>. The in-plane correlation length at the surface is a factor of ~6 shorter than the bulk, demonstrating that the correlation length strongly varies as a function of depth from the surface. **Fig. 2b** highlights the surface sensitivity of our experiment by comparing the fluence dependence of the OTR and OBP which shows that the surface scattering quickly saturates at much lower fluences. The observed ~80% decrease above 4 mJ/cm<sup>2</sup> excitation indicates the near-complete melting of orbital ordering at the surface layer. In **Fig. 2c,d**, we show the dynamics of the peak amplitude and the width of the OTR in the K direction, obtained by fitting the data at L=0.2 with a Lorentzian line shape (see methods). The OTR intensity is rapidly suppressed upon photoexcitation, similar to the OBP. However, the width of the remaining OTR dramatically increases by up to 70%, in opposition to the narrowing observed at the OBP.

Before reconciling the OBP and OTR data, we first examine the oscillations that are also observed to modulate the OTR amplitude and width. **Figure 3a** shows the frequency dependence of the oscillations as a function of pump fluence. At low excitation fluence, a single frequency response at  $\omega = 2.8 \text{ THz}$  is observed. As the fluence is increased the amplitude of this mode is suppressed and a new peak emerges at the second harmonic, ~5.6 THz. This change coincides with the suppression of the OTR scattering. In charge density wave compounds, the sudden appearance of higher frequency oscillations is attributed to the order parameter oscillating around a high symmetry state<sup>22–24</sup>. As the peak intensity is proportional to the square of the order parameter, the peak oscillates at twice the frequency of the actual motion. However, we do not believe this to be the case here. Firstly, before the frequency increases, the order parameter frequency should first soften as the curvature of the free energy potential is reduced, which is not seen. Secondly, it would be highly coincidental if the high symmetry potential had the same curvature as the symmetry broken state. Finally, the oscillation does not modulate the OBP measured here, which should also be sensitive to the order parameter.

Instead, we suggest that the observed oscillation is due to a spectator phonon. The 2.8 THz mode seen here can be assigned to the motion of the La/Sr ions<sup>25</sup>, which do not appreciably change position during the phase transition and are thus not directly related to the order parameter<sup>26</sup>. The reduction in symmetry

from  $I4/mmm$  at high temperatures to  $Cmmm$  in the orbitally ordered state causes a large increase in the number of Raman active modes. Phonons from the M or LD points of the high symmetry phase get mapped onto the  $\Gamma$ -point, increasing the number of modes from Raman active modes from six to 39. These new 'back-folded' modes can be considered spectator modes<sup>19,21</sup> of the phase transition. As the manganites have strong electron-phonon coupling, ultrafast electronic excitation can be expected to drive large amplitude coherent oscillations of these new modes<sup>21,27</sup> and X-ray scattering from these back-folded modes will then modulate the intensity at the same wavevector as the orbital ordering.

Unlike in equilibrium, where the scattering at the orbital ordering wavevector is only proportional to the squared magnitude of the order parameter, the out-of-equilibrium scattering will now contain an additional contribution from the coherent phonon. If the order parameter is not suppressed, X-rays scattered from the orbital order and the phonon will interfere, resulting in a term contributing to the scattering which is linear in the phonon displacement. However, if the orbital order is fully suppressed during the dynamics, the interference is lost and the mode appears at the second harmonic, as is the case for phonon modes at a finite wavevector<sup>28</sup>. Excellent agreement with the data and a simple model for the phonon supports this assignment (see **Fig. 2c** and methods).

Further evidence that the oscillation is not directly related to the order parameter comes from the momentum dependence of the mode. In **Fig. 3b,c**, we extract the amplitude of the phonon contribution to the OTR intensity in the K and L directions and compare it to the scattering from the OTR scattering in equilibrium (methods). We find that the region modulated is narrower in both the in-plane and out-of-plane directions showing the oscillations are more delocalised in real space. This is consistent with the fact that the structure formed by the La/Sr cage is known to have a higher correlation length than the orbital order<sup>9,10</sup>. As a result, the dynamics of the scattering around the OTR are governed by at least two different processes with different widths in reciprocal space, one corresponding to the dynamics of the order parameter, and the other to the coherent phonon. The effective width of the OTR, when fitted with a single peak function, is then modulated when the relative amplitude of the two different components changes.

In **Fig. 3c** we fit the dynamics of the peak and width to remove the influence of the phonon and show the case for  $2 \text{ mJ cm}^{-2}$  excitation (see **extended data figure 2** for all fluences). We find that the amplitude of the OTR follows an overdamped response consistent with what is observed optically<sup>21</sup>, decreasing with a time-constant of the order of 70 fs depending on fluence (see **extended data figure 3**). Interestingly, we see that the width increases with a slower component not seen in the amplitude data but is delayed by a few tens of femtoseconds relative to the amplitude suppression, suggesting the change in correlation length at the surface is a slower and more complex phenomena than the reduction in the amplitude.

To understand the melting process and the change in correlation in more detail, we look at a larger region of reciprocal space. **Figure 4a,b** shows the region around the OTR 1 ps after pumping at  $12 \text{ mJ/cm}^2$ . In addition to the suppression of the OTR (blue), there is a large increase in diffuse scattering spanning a much large region of the reciprocal space. The intensity is peaked along the line  $[H, K] = [2-K, K]$  and is extended in L, increasing towards the (020) structural peak. This indicates that a broad distribution of acoustic phonons is generated after photoexcitation. **Fig. 4c** shows the dynamics of the diffuse scattering at various points in momentum space, showing that the rise time depends strongly on momentum. This momentum dependence of the fitted rise time is shown in **Fig. 4d,e** for selected cuts through reciprocal space. The dynamics are fastest closest to the (020) structural peak, and become slower when moving

away from the  $[H, K]=[2-K, K]$  diagonal or in L. Although we do not measure closer to the (020) peak, we find that the fastest increase in diffuse signal (115 fs) is already comparable to the  $\sim 50$  fs, resolution limited, decay time of the orbital order (dashed line in **Fig. 4d**). The similarities in timescales suggest that the loss of long-range orbital order and rapid generation of incoherent phonons are driven through the same electronic mechanism.

The observation of the diffuse signal rapidly appearing close to the (020) peak and expanding to large momentum at longer delays is surprising. In equilibrium, the intensity of the diffuse scattering signal is determined by the number of phonons in the mode, which is determined by the temperature. As a result, the low energy acoustic phonons close to the zone centre dominate the diffuse scattering. Thus, our measurements would be consistent with a rapidly thermalized lattice. However, on the ultrafast timescale, it is difficult to get energy into these modes so fast. Photoexcited electrons typically relax through scattering with high energy acoustic modes at the Brillouin zone boundary first and then these modes decay into phonons closer to the  $\Gamma$ -point by slower phonon-phonon scattering events as seen in charge density wave compounds<sup>13,29</sup>. This is the opposite to what we observe.

Instead, we suggest that the diffuse scattering results from near zone-centre optical phonons, which have much higher energy and can be directly excited by the laser. The slower broadening of the diffuse distribution in momentum space is consistent with a localization of these long-range distortions into disordered local polarons, similar to what has been proposed in SnSe<sup>30</sup>, but on a significantly faster timescale. Polarons are a key component of the physics of the manganites<sup>31–33</sup> and thus, it seems likely that incoherent polaron formation drives the loss of long-range orbital ordering. However, true verification of the polaronic nature of this scattering, rather than just thermal disorder, would require knowledge of the phase of the scattered X-rays which we do not get from an intensity measurement. This may be possible in the future with coherent scattering techniques<sup>34</sup>.

The picture that emerges for melting of orbital ordering is as follows: optical excitation rapidly suppresses orbital order at the surface, as measured through the OTR. Initially, this results in a suppression of the amplitude of the order parameter, without a change in heterogeneity but within a few tens of femtoseconds, the correlation length also decreases. The decrease in correlation length is likely driven by the formation of local incoherent and disordered polarons and points towards photoinduced orbital order melting as an order-disorder transition<sup>35</sup>. The reason why the bulk correlation length, as measured by the OBP, increases is because it is measuring a much deeper volume which is heterogeneous before the material is excited. The OBP averages the correlation length over a depth of region of 100 nm, but regions with shorter correlation length are found at the surface. When the scattering from these regions is suppressed, the average correlation length of the remaining volume effectively increases, even though no region actually undergoes an increase in correlation length.

The proposed mechanism contrasts with the coherent mechanism previously proposed for the phase transition<sup>16</sup> and instead shares many similarities to the dynamics observed in VO<sub>2</sub><sup>36</sup>. The non-thermal polaron distribution immediately after excitation is also reminiscent of recent observations in VO<sub>2</sub>, suggesting that control strategies that exploit transient disorder may also be applicable for optimising transitions in the manganites<sup>37</sup>. Although the order parameter dynamic we observe is incoherent, the lattice dynamics of the spectator modes can remain coherent throughout the melting process. This implies that the disappearance of vibrational modes in optical experiments does not necessarily mean vibrational

coherence is lost<sup>38</sup>, but rather becomes undetectable as the mode is no-longer optically active, and that vibrational coherence can be maintained across a phase transition.

An interesting question remains as to whether resonant IR excitation, which has also been shown to melt orbital ordering<sup>2,39</sup>, does so along the same disordered pathway as optical excitation or if the process is more coherent. The non-linear phononics mechanism proposed to explain light-induced effects in the manganites and cuprates, assumes that long-wavelength Raman active modes are responsible for the light-induced change in material properties<sup>40</sup>. Such a mechanism would not directly induce the diffuse scattering seen here. A surface scattering measurement under mid-IR excitation may then help elucidate the different nature of phonon drive phase transitions and resolve penetration depth issues in light-induced superconductivity<sup>41</sup>.

We stress that the ability to directly probe heterogeneity has been key to making these observations. Specifically, interpreting the Bragg peak data at face value gives an incorrect picture of the physical processes occurring. In our case, the sample started in a heterogenous state, but pump-probe penetration depth mismatch will always result in a heterogeneously excited volume, which requires modelling to interpret. For example, experiments have observed that ultrafast melting occurs without peak broadening and attributed it to the absence of topological defects<sup>1</sup>. Our results indicate the broadening may still occur at the melted surface but is hidden from bulk probes even if the penetration depth is nominally matched. Thus, methods to resolve light-induced heterogeneity will be vital to accurately interpret dynamics in quantum materials.

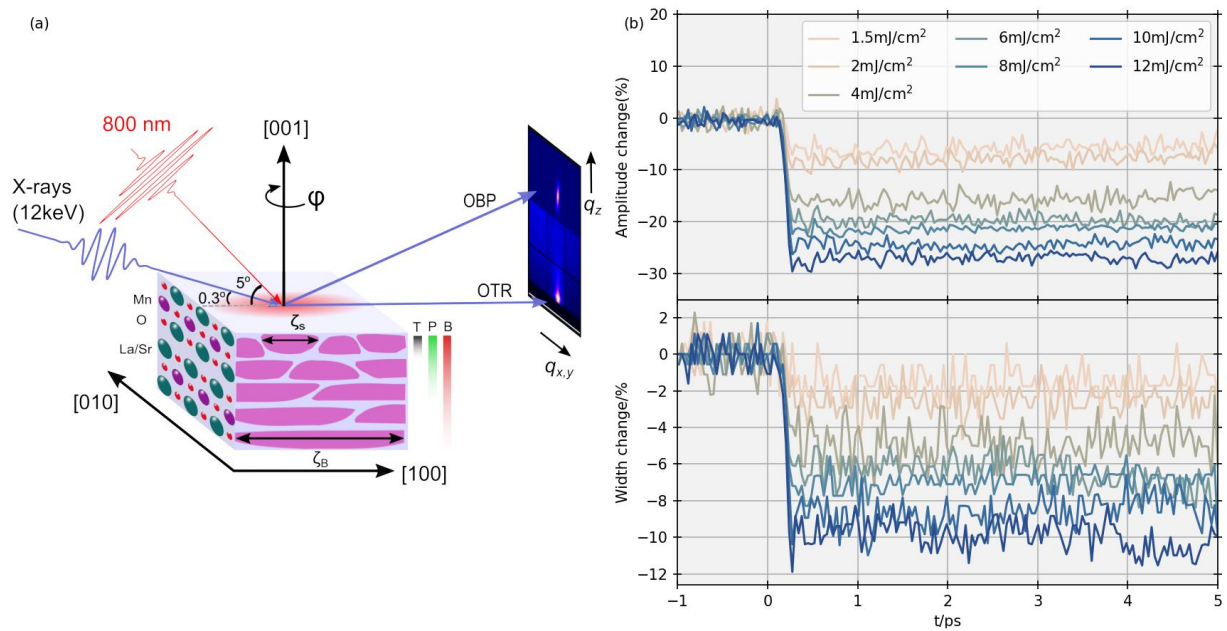


**Figure 1 Experimental setup and dynamics of bulk orbital order.** **a** Schematic of the experimental setup to measure the  $(2.25, -0.25, 2)$  orbital Bragg peak and  $(2.25, -0.25, L)$  orbital truncation rod. Measurements were performed at  $0.3^\circ$  grazing incidence and switching between the OBP and OTR involved changing the angle  $\phi$ .  $\zeta_s, \zeta_B$  indicate the difference in correlation length at the surface and bulk respectively. T,P,B indicate the depth probed by the truncation rod (T), the depth pumped by the laser (P) and the depth probed by the Bragg peak (B) **b** Dynamics of the amplitude and width along the L direction after photoexcitation. In both cases, the width and amplitude parameters were found to change within the temporal resolution. The narrowing is confirmed in a full reciprocal space map taken at 1 ps delay and shown in **extended data figure 1**.

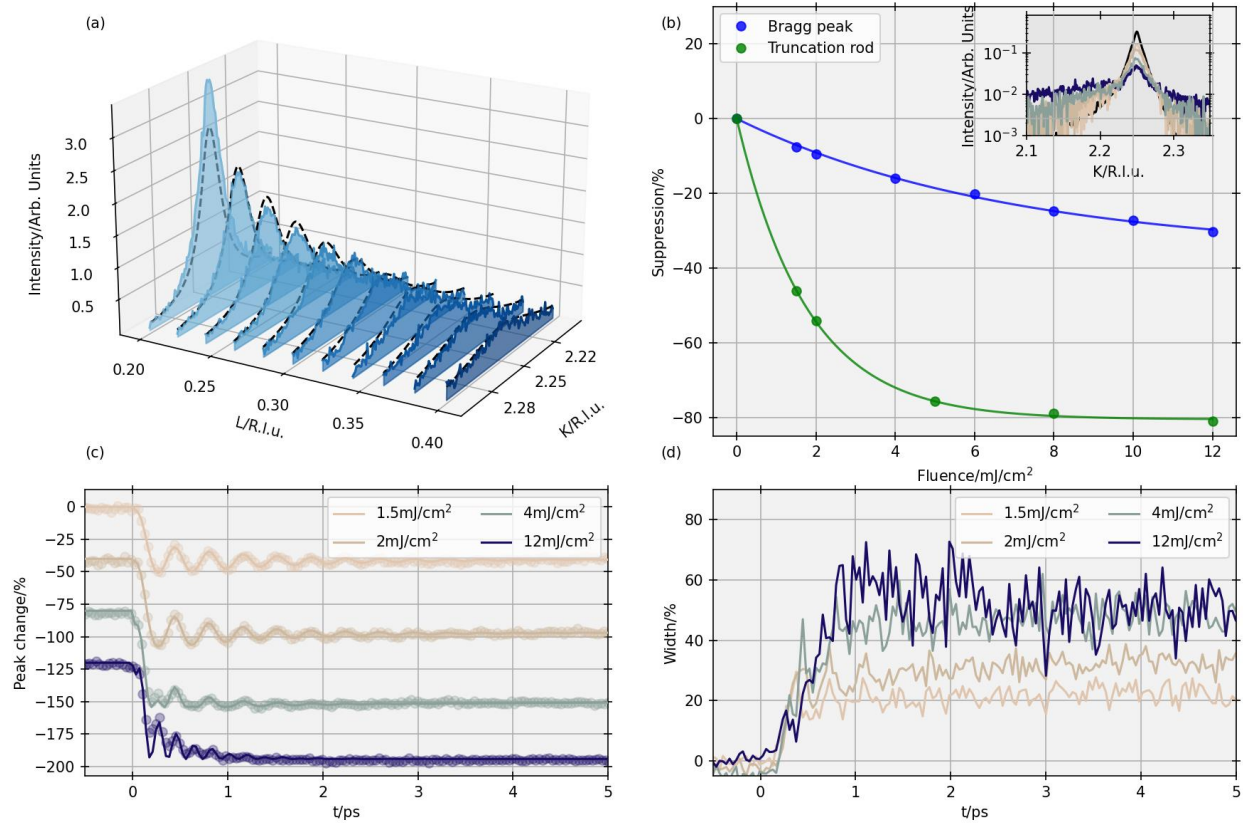


**Figure 2 Orbital ordering melting dynamics at the surface measured through the orbital truncation rod (OTR).** **a** Measurement of the OTR in the KL plane. L is parallel to the surface normal. Dashed lines are fits based on modelling the surface scattering (see methods). **b** Fluence dependence of the OBP and OTR obtained from integrating a small ROI in reciprocal space around the peak scattering in each case, 1 ps after excitation, solid lines are guides to the eye. Insert shows a cut of the OTR along K at L=0.2, 1 ps after excitation. Dynamics of the peak intensity **c** and width **d** along the K direction of the OTR measured at L=0.2 obtained from fitting the experimental data. Solid lines in **c** are fits obtained with a simple spectator model for the phonon (see methods and **extended data figures 2, 3**). Unlike the OBP, the OTR broadens in width when excited indicating the correlation length has decreased.



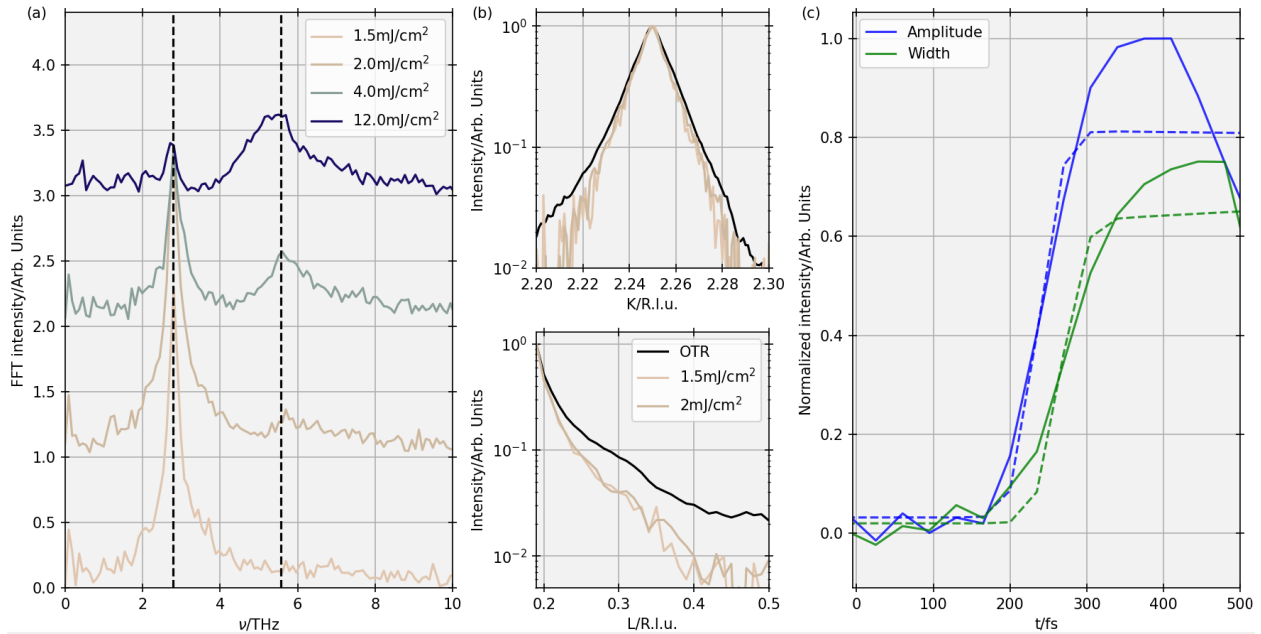


**Figure 3 Phonon dynamics during the melting of orbital order.** **a** Fourier transform of the optical phonon oscillations modulating the OTR amplitude observed in Fig. 2c after background subtraction. At low fluences, the oscillations are observed at 2.8 THz. As the fluence increases, a second peak grows at the second harmonic of the fundamental. Dashed lines indicate the fundamental and its second harmonic. During melting, only a small shift in the phonon frequency and lifetime are found (see extended data 3). **b** The phonon amplitude as a function of reciprocal space coordinate. The phonon peak is narrower in reciprocal space, suggesting it more delocalised in real space. **c** Comparison of the width and amplitude dynamics of the OTR following 2 mJ/cm<sup>2</sup> excitation. The dashed line indicates the dynamics of the orbital order after subtracting the phonon component from each dynamic. The width dynamics are slower to change than the peak indicating that the magnitude of the distortion is first reduced and then the size of the ordered regions then contracts.

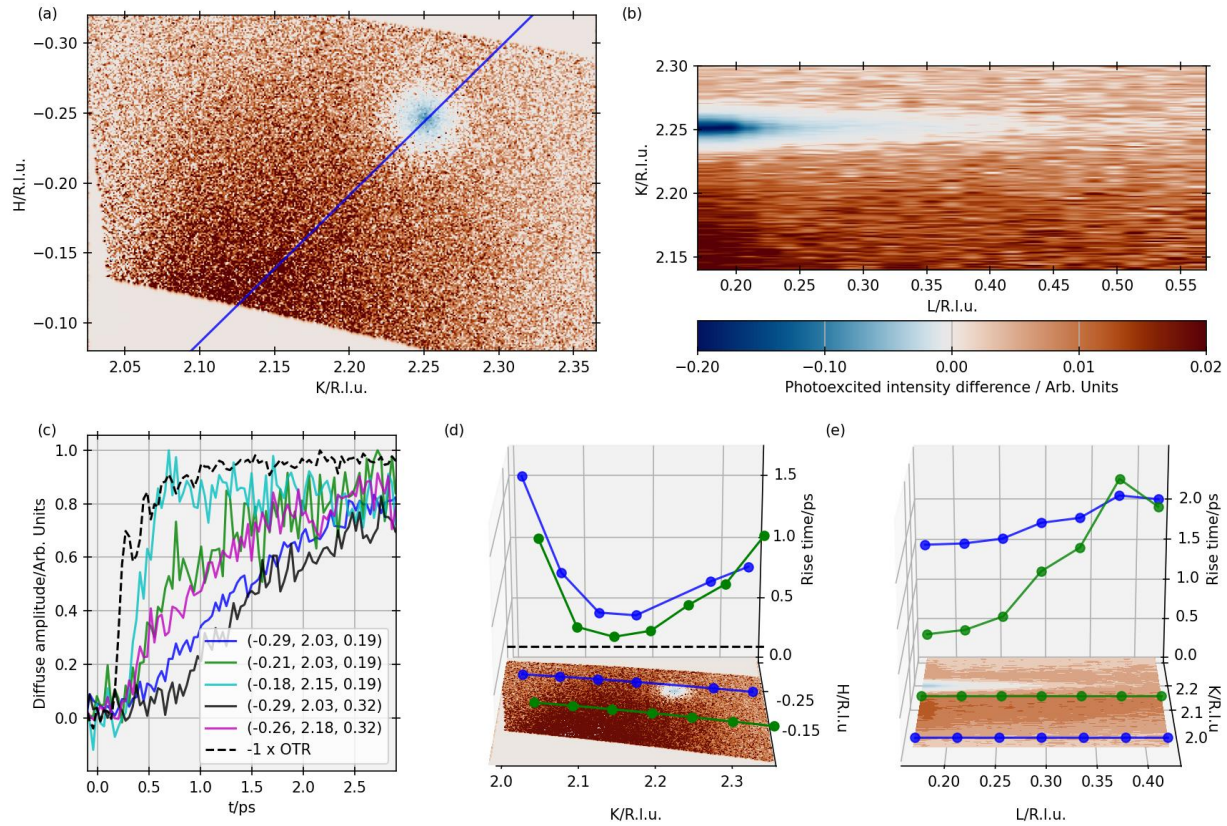


**Figure 4 Polaron formation during the melting of orbital order.** Cuts in reciprocal space of the change in scattering around the OTR in the HK plane at  $L = 0.2$  **a**, and cut along the Line  $[H, K]=[2-K, K]$  (blue line in **a**) in the L direction **b** In addition to the suppression of the OTR (blue) a large region of diffuse scattering appears which increases in intensity as the (020) structural peak is approached **c** Dynamics at selected points in the diffuse scattering map showing that the dynamics are strongly dependent on momentum. Suppression of OTR is plotted as positive signal for comparison. Extracted timescales based on fitting the diffuse dynamics with  $I(k, t) = A_k(1 - e^{-\frac{t}{\tau_k}})$  for delays greater than zero in the HK plane at  $L=0.2$  **d** and in the KL plane at  $H \sim -0.25$  **e**. Dynamics are fastest along the line  $[H, K]=[2-K, K]$  and reduces further as the (020) structural peak is approached. Dynamics are also slower in the L direction.

## Methods

### Experimental setup

Experiments were performed at the SwissFEL Bernina instrument<sup>42</sup>. Single crystal samples were grown by the floating zone method and were cleaved in air to expose a (001) surface normal and mounted onto a 6-circle diffractometer. To achieve surface sensitivity, experiments were performed at a grazing incidence angle of 0.3° with a non-resonant photon energy of 12 keV, which was monochromatised to a 1.7 eV bandwidth. The base temperature of 180 K to avoid generation of any meta-stable states, which have been observed in lab-based optical experiments for temperatures below 140 K and to ensure the sample recovers between pump pulses. X-rays were focused to a spot of  $2 \times 100 \mu\text{m}^2$  onto the sample (normal incidence spot size).

The system was pumped with 800 nm laser pulses incident at 5° with a beam spot of  $60 \times 2000 \mu\text{m}^2$ . The estimated time resolution of the setup was 70 fs.

In this geometry, the calculated X-ray penetration depth (110 nm) is nominally well matched to the optically pumped depth (116 nm) based on literature values<sup>43,44</sup> for the optical and X-ray constants.

We performed two types of measurements, time-scans at fixed detector settings, which captured cuts primarily in the KL plane of the orbital order and orbital truncation rod, and reciprocal space maps at fixed delays which scanned the sample around the surface normal, keeping the angle of incidence fixed.

Measurements of the OBP and OTR were performed at different  $\phi$  angles (see Fig 1) and with the detector rotated to the appropriate angles. The incident angle did not change in this geometry.

### Pump and probe penetration depth

The X-ray penetration depth was calculated using the data in Ref. <sup>44</sup>. The penetration of the pump was calculated use a refractive index of  $1.36+0.37i$ , obtained from the reflectivity data of Ishikawa et al.<sup>43</sup> (180 K and for S-polarized, 800 nm beam). Taking into account refraction of the pump, the resulting in a penetration depth of 116 nm is obtained.

### Calculation of the in-plane correlation length and surface roughness from the orbital truncation rod

The intensity of the orbital truncation rod can be expressed as<sup>35</sup>

$$I(K, L) = \left| \left( \frac{f(H, K, L)}{1 - e^{2i\pi L - \alpha}} \right) \right|^2 \frac{A}{\sin \theta} \frac{L^2 r}{32(\Delta H^2 + \Delta K^2 + 4\pi^2 L^4 r^2)^{\frac{3}{2}}}$$

Where,  $r = \frac{(2\sigma)^2}{c_r}$ ,  $\alpha = \frac{\mu c}{2} \left( \frac{1}{\sin \alpha_i} + \frac{1}{L_c^\lambda \sin \alpha_i} \right)$ ,  $\sigma$  is the surface roughness,  $c_r$  is the phase-slip length.  $\alpha_i = 0.3^\circ$  is the incident angle,  $\mu$  is the absorption coefficient,  $c$  is the lattice constant along the out of plane direction and  $\lambda$  is the X-ray wavelength.  $f(H, K, L)$  is the scattering factor of the orbital ordering supercell.

After averaging the orbital ordering domain configurations for  $f(H, K, L)$ , the above equation can be approximated by a Lorentzian function of K in the KL plane:

$$I(K, L) = \left| \left( \frac{1}{1 - e^{2i\pi L - \alpha}} \right) \right|^2 A \frac{L^2 r}{8(K - K_0)^2 + 2\pi^2 L^4 r^2}$$

We performed a reciprocal space map of the orbital order to build up a three-dimensional dataset to get the intensity as a function of H,K,L. We then integrate along the H direction to get a two-dimensional representation. The dataset is fitted with two parameters for all L values: A, representing the amplitude of the distortion and  $r=0.039$ , after a background has been removed.

The shape of the rod at a fixed L can be described with a Lorentzian line shape:

$$I(K, L = 0.2) = \frac{\Gamma A'}{(K - K_0)^2 + \frac{\Gamma^2}{4}}$$

From which we can extract an in-plane correlation length:

$$\xi_s = a/2\pi\Gamma \sim 40\text{\AA}$$

Where  $a = 3.853\text{\AA}$  is the in-plane lattice constant.

In the time dependent data presented in Fig. 2, we fit the area  $A'$  and width  $\Gamma$  as a function of pump probe delay at the L=0.2 point, but plot the peak intensity  $\frac{A'}{\Gamma}$  and  $\Gamma$ .  $A'$  is plotted in **Extended data Figure 2**.

### Fitting the Orbital Bragg peak

To determine the correlation lengths of the bulk orbital order from the OBP, we carried out a reciprocal space scan as mentioned in the main text. To extract the in-plane correlation length, we selected the (H K 2) map and fit the data in H and K directions using a Lorentzian profile as above. To this end, the data were first converted from reciprocal space unit (*r.l.u*) into *q*-space and then fitted. The correlation length of the OBP, is then the reciprocal of the extracted width (FWHM). This yielded a value of 250 Å for the in-plane correlation length.

For the out-of-plane correlation length, each image from the RSM in the HK plane was binned in H or K direction and maximum of the resulting peak was taken as a function of L and then fit with the same functional.

For the time-resolved scans, on the other hand, the CCD was fixed and we, therefore, took a cut through the OBP along (-2.25 K 2) and (H 2.25 2), respectively, and fit the traces at each time delay.

### Spectator modes

To describe the change in the phonon frequency we present a simple toy model for the “spectator mode”, which is not meant to capture the true structural changes, but highlights how the phonon frequency shifts to the second harmonic.

We take simplified unit cell consisting of only La/Sr ions located at (0,0,0) and the Mn ions at ( $\frac{1}{2}$ ,  $\frac{1}{2}$ , 0). We assume that the order parameter can be represented by a displacement of the Mn ions by an amount  $\eta$ . In equilibrium, this will generate orbital order peaks whose intensity,  $I_{00}$ , will scale as  $I_{00} \propto \eta^2$  for small displacements.

If the La/Sr ions remain at the high symmetry position, they do not contribute to any scattering to the  $I_{OO}$  peaks. However, the displacement of the Mn ions modifies the environment of the La/Sr ions, so that these atoms can also become Raman active, and can thus move away from their high symmetry points. If the La/Sr ions oscillate by an amount  $\beta$  at the same wavevector as the order parameter, the orbital order intensity will then be given by the coherent sum of the two scattering factors or

$$I_{OO} \propto (\eta + \beta)^2$$

We assume that the La/Sr ions are initially in the high symmetry positions and coherent oscillations are generated with a sine-like phase such that  $\beta(t) = \beta_0 \sin \omega_p t$ , i.e. they oscillate around their equilibrium position, rather than a non-equilibrium position. We then assume that the order parameter follows a non-oscillatory dynamic,  $\eta(t)$ . The change in superlattice intensity can then be written as

$$\begin{aligned} \Delta I_{SL} &= \eta^2(t) + \beta^2(t) + 2\eta(t)\beta(t) - \eta_0^2 \\ &= \eta^2(t) - \eta_0^2 + \frac{\beta_0^2}{2} + 2\eta(t)\beta_0 \sin \omega_p t - \frac{\beta_0^2}{2} \cos 2\omega_p t \end{aligned}$$

Here it can be seen that if  $\eta(t)$  remains finite, the orbital order intensity will oscillate at  $\omega$ , whereas if the order parameter is suppressed  $\eta(t) \rightarrow 0$  the frequency changes the  $2\omega$ .

To fit the dynamics of the intensity, we assume that in addition to the scattering from the order parameter  $\eta$  and the phonon  $\beta$  there is some incoherent background,  $B$ , which can be noise on the detector or other scattering which is independent of any pump parameter. This gives the measured intensity as

$$I_{OO} \propto (\eta + \beta)^2 + B$$

The intensity before pumping is given by

$$I_{OO}(-t) \propto \eta_0^2 + B$$

Where  $\eta_0$  is the order parameter value before pumping.

The measured relative change is then given as

$$\frac{\Delta I_{OO}}{I_{OO}(-t)} = \frac{(\eta + \beta)^2 - \eta_0^2}{\eta_0^2 + B}$$

When then assume that  $\eta(t)$  has the same functional form as extracted from optical measurements<sup>21</sup>

$$\eta(t) = \eta_0 \left( 1 - \frac{\delta\eta}{\eta_0}(t) \right)$$

Where

$$\frac{\delta\eta}{\eta_0}(t) = f(1 - e^{-t/\tau_d})e^{-t/\tau_r}$$

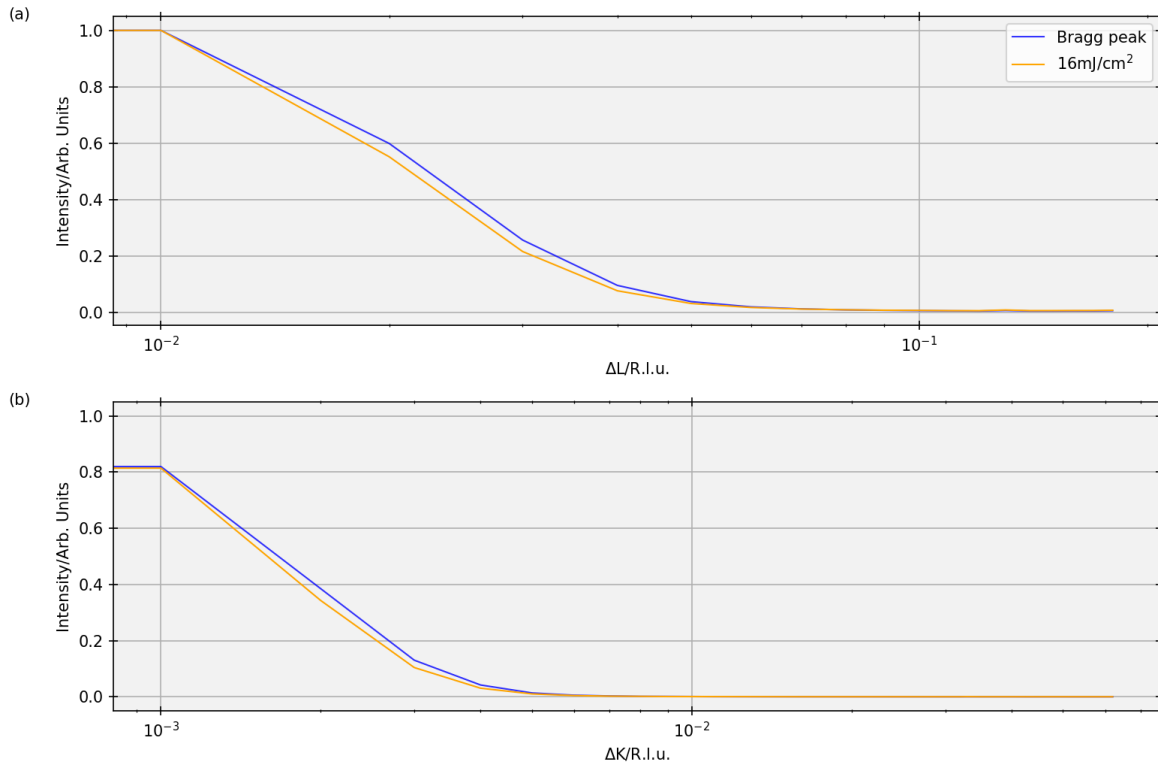
and  $\tau_d$  and  $\tau_r$  are the decay and recovery time of the order and  $f$  is the melt fraction. Substituting this into the equation for the relative change in superlattice intensity gives

$$\frac{\Delta I_{SL}}{I_{SL}(-t)} = \frac{\eta_0^2}{\eta_0^2 + B} \left[ - \left( 2 - \frac{\delta\eta}{\eta_0} \right) \frac{\delta\eta}{\eta_0} + \frac{\beta_0^2}{2\eta_0^2} e^{-\frac{2t}{\tau_p}} (1 - \cos 2\omega_p t) + \frac{2\beta_0}{\eta_0} \left( 1 - \frac{\delta\eta}{\eta_0} \right) e^{-t/\tau_p} \sin \omega_p t \right]. \quad (1)$$

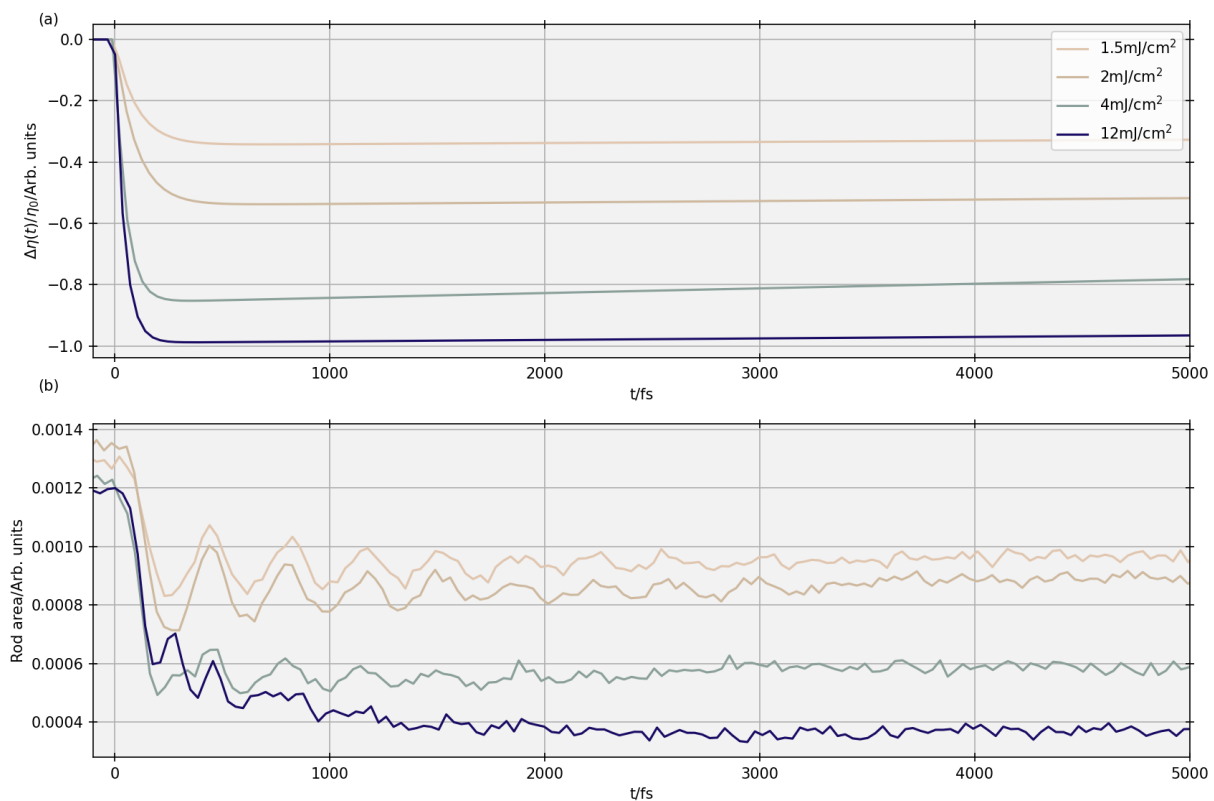
This model is then fitted to the peak intensity shown in Fig 2c. The corresponding dynamics for the order parameter are plotted in **extended data figure 2**. The fluence dependent fit parameters for the fit parameters are shown in **extended data figure 3**. Note that the parameter B is the same for all fluences.

We note that unlike Ref 13, we do not need to include a time-dependent dephasing constant to fit our data because the order parameter dynamics and the oscillations are not coupled.

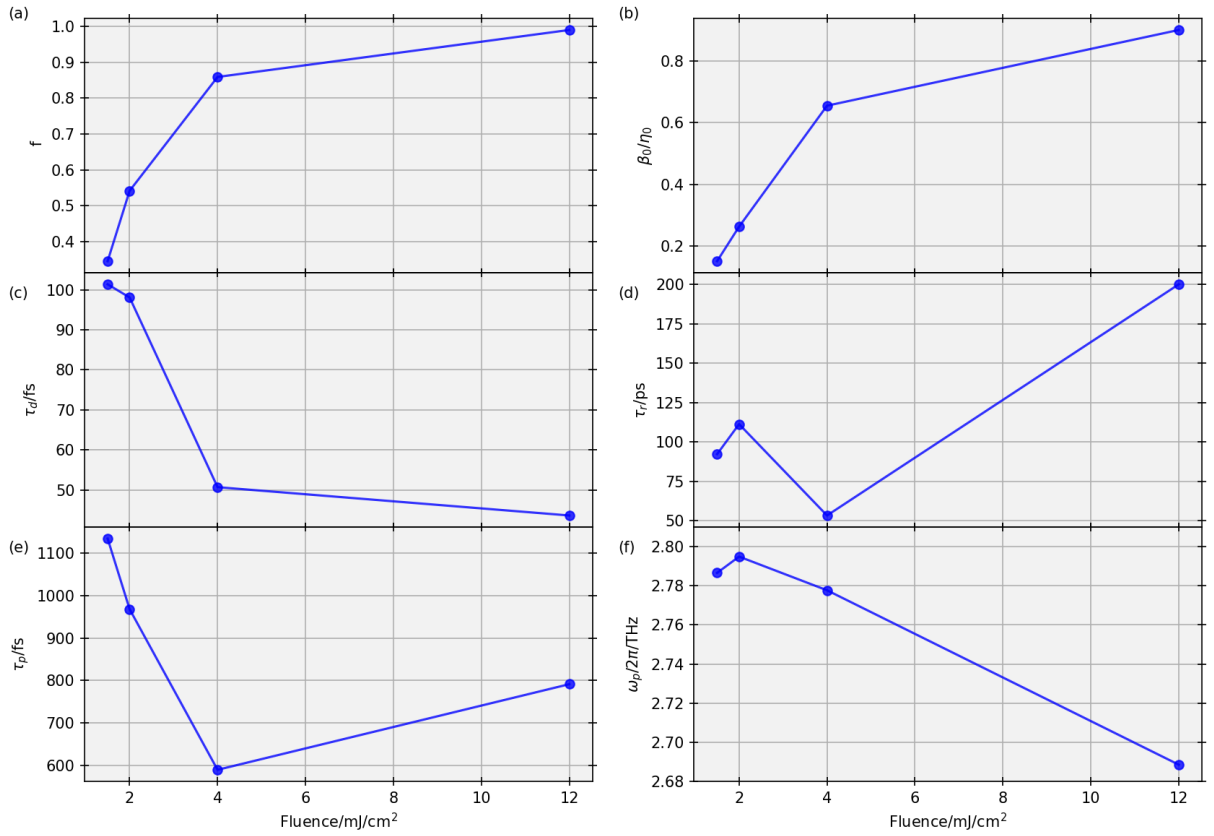
Although the phonon is only observed on the OTR, it is not a surface phonon as it is also seen in optical reflectivity data<sup>21</sup> and is seen in bulk Bragg peaks in other materials<sup>18-20</sup>. The lack of phonon in the OBP measured here, indicates the phonon has a dispersion along L, i.e. bulk peaks at different wavevectors are likely to show the phonon.



**Extended data figure 1 Half width of the (-0.25, 2.25, 2) Orbital Bragg Peak after excitation with 16 mJ/cm<sup>2</sup> and at 1 ps delay.** The data in Fig. 1b comes from fitting a slice of reciprocal space slightly off centre due to the fixed angle of the detector. Here we performed a measurement of the full reciprocal space around the OBP to ensure the narrowing was not due to the movement of the peak relative to the detection plane and plot the half width on a semi-log scale. Here we still observe a narrowing of 9% along out-of-plane (L) and 6% in-plane (K) directions, respectively, demonstrating the transient narrowing observed is real.

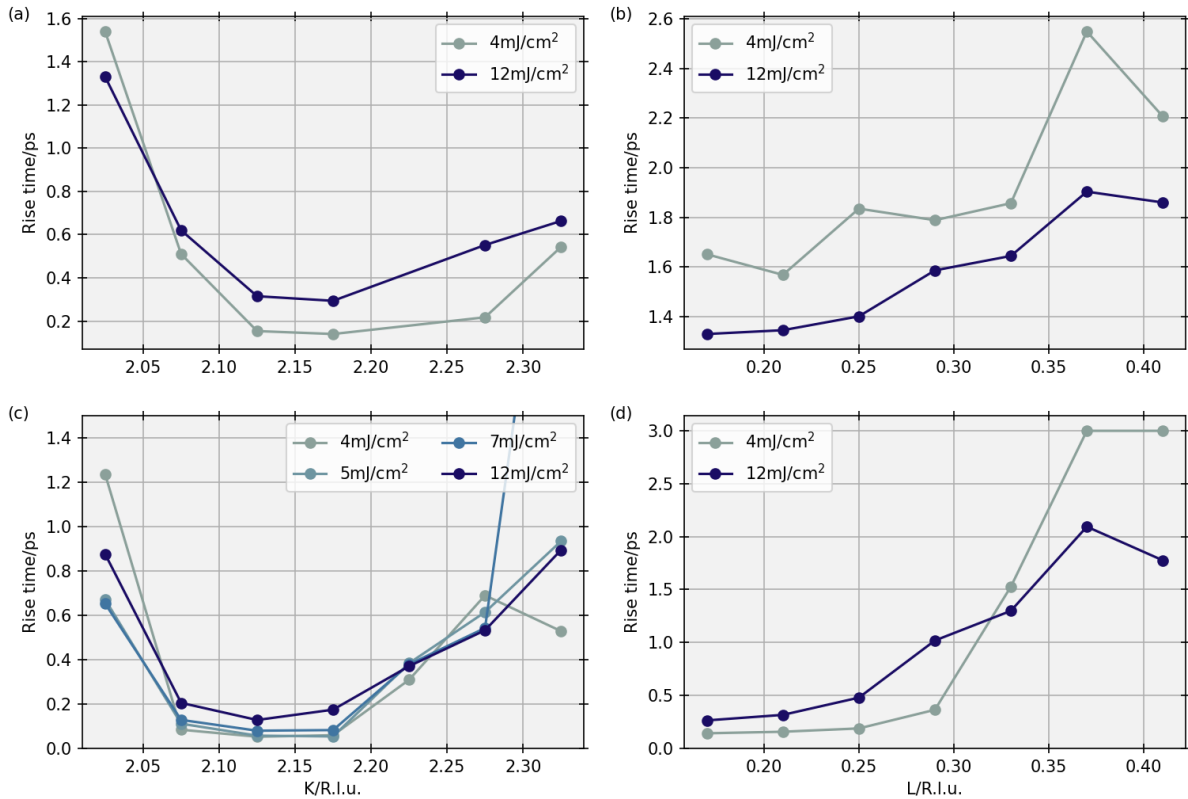


**Extended data Figure 2: Extraction of order parameter from the orbital truncation rod.** **a** Shows the extracted change in order parameter from the change in amplitude of the orbital truncation rod. **b** plots the rod area parameter,  $A'$ , which is proportional to the integrated area of the Lorentzian fitted to the transient data.



**Extended data figure 3:** Fit parameters for the order parameter and phonon model. The parameters are defined in equation 1.





**Extended data Figure 4: Comparison of the rise time of the diffuse scattering resulting from different fluence excitation.** While diffuse scattering was observed for lower fluences, the signal to noise ratio prevented accurate determination of the time constants.

### Extracting the phonon amplitudes in the KL plane

We used two methods to extract the phonon amplitude. In the first method, we used a modified form of the model above, to take into account the increase in diffuse scattering, to fit the phonon amplitude at each point in the measured LK plane.

In the second method we performed a principal component analysis of the data. We found that three different temporal dynamics could reproduce the dynamics in the LK plane and from these three components we extracted the phonon intensity as a function of momentum.

Both processes gave very similar results, with the latter being used in the paper.

### Acknowledgements

We acknowledge the Paul Scherrer Institut, Villigen, Switzerland, for provision of beamtime at the Bernina beamline of SwissFEL. S.W acknowledges support from Carlsbergfondet (CF20-0169). We thank the Danish Agency for Science, Technology, and Innovation for funding the instrument center DanScatt for travel support. We also thank Jakob Voldum Ahlburg, the Center for Integrated Materials Research (iMAT) at Aarhus University, and Huang Shih-Wen for support on sample characterisation. Xiang Li and Xuerong Liu acknowledge support from the MOST of China under Grant No. 2022YFA1603900.

## Author Contributions

S.E.W and Xuerong Liu conceived of the project.

Samples were grown and characterized by D.P.

K.M.S and N.A prepared samples for experiments.

K.M.S, M.M, D.P.S, N.A, M.B, S.E.W performed the experiment with support from Xin Liu, D.B, M.S, Y.D, H.T.L and, R. M. Data analysis was performed by M.M, X.Li, Xuerong Liu and K.M.S.

## References

1. Lee, W. S. *et al.* Phase fluctuations and the absence of topological defects in a photo-excited charge-ordered nickelate. *Nat. Commun.* **3**, 838 (2012).
2. Först, M. *et al.* Driving magnetic order in a manganite by ultrafast lattice excitation. *Phys. Rev. B* **84**, 241104 (2011).
3. Otto, M. R. *et al.* How optical excitation controls the structure and properties of vanadium dioxide. *PNAS* **116**, 450–455 (2018).
4. Sood, A. *et al.* Universal phase dynamics in VO<sub>2</sub> switches revealed by ultrafast operando diffraction. *Science* **373**, 352–355 (2021).
5. Wandel, S. *et al.* Enhanced charge density wave coherence in a light-quenched, high-temperature superconductor. *Science* **376**, 860–864 (2022).
6. Ning, H. *et al.* Dynamical decoding of the competition between charge density waves in a kagome superconductor. Preprint at <https://doi.org/10.48550/arXiv.2403.03169> (2024).
7. Frenken, J. W. M. & Veen, J. F. van der. Observation of Surface Melting. *Phys. Rev. Lett.* **54**, 134–137 (1985).
8. Doi, S. & Takahashi, I. Critical behaviour of the SrTiO<sub>3</sub>(001) surface at the structural phase transition. *Philos. Mag. A* **80**, 1889–1899 (2000).
9. Wakabayashi, Y. *et al.* Surface effects on the orbital order in the single-layered manganite La<sub>0.5</sub>Sr<sub>1.5</sub>MnO<sub>4</sub>. *Nat. Mater.* **6**, 972–976 (2007).

10. Wilkins, S. B. *et al.* Surface melting of electronic order in  $\text{La}_{0.5}\text{Sr}_{1.5}\text{MnO}_4$ . *Phys. Rev. B* **84**, 165103 (2011).
11. Johnson, A. S. *et al.* Ultrafast X-ray imaging of the light-induced phase transition in  $\text{VO}_2$ . *Nat. Phys.* **19**, 215–220 (2023).
12. Sternbach, A. J. *et al.* Inhomogeneous Photosusceptibility of  $\text{VO}_2$  Films at the Nanoscale. *Phys. Rev. Lett.* **132**, 186903 (2024).
13. Kurtz, F. *et al.* Non-thermal phonon dynamics and a quenched exciton condensate probed by surface-sensitive electron diffraction. *Nat. Mater.* 1–8 (2024) doi:10.1038/s41563-024-01880-6.
14. Tung, I.-C. *et al.* Anisotropic structural dynamics of monolayer crystals revealed by femtosecond surface X-ray scattering. *Nat. Photonics* **13**, 425–430 (2019).
15. Zhou, S. Y. *et al.* Glass-like recovery of antiferromagnetic spin ordering in a photo-excited manganite  $\text{Pr}_{0.7}\text{Ca}_{0.3}\text{MnO}_3$ . *Sci. Rep.* **4**, 4050 (2014).
16. Polli, D. *et al.* Coherent orbital waves in the photo-induced insulator-metal dynamics of a magnetoresistive manganite. *Nat. Mater.* **6**, 643–7 (2007).
17. Matsuzaki, H. *et al.* Detecting charge and lattice dynamics in photoinduced charge-order melting in perovskite-type manganites using a 30-femtosecond time resolution. *Phys. Rev. B - Condens. Matter Mater. Phys.* **79**, 235131 (2009).
18. Porer, M. *et al.* Correlations between electronic order and structural distortions and their ultrafast dynamics in the single-layer manganite  $\text{Pr}_{0.5}\text{Ca}_{1.5}\text{MnO}_4$ . *Phys. Rev. B* **101**, 75119 (2020).
19. Beaud, P. *et al.* A time-dependent order parameter for ultrafast photoinduced phase transitions. *Nat. Mater.* **13**, 923–927 (2014).
20. Rettig, L. *et al.* Disentangling transient charge order from structural dynamics contributions during coherent atomic motion studied by ultrafast resonant x-ray diffraction. *Phys. Rev. B* **99**, 132302 (2019).

21. Perez-Salinas, D., Johnson, A. S., Prabhakaran, D. & Wall, S. Multi-mode excitation drives disorder during the ultrafast melting of a C4-symmetry-broken phase. *Nat. Commun.* **13**, 238 (2022).
22. Duan, S. *et al.* Optical manipulation of electronic dimensionality in a quantum material. *Nature* **595**, 239–244 (2021).
23. Huber, T. *et al.* Coherent structural dynamics of a prototypical charge-density-wave-to-metal transition. *Phys. Rev. Lett.* **113**, 026401 (2014).
24. Trigo, M. *et al.* Coherent order parameter dynamics in SmTe<sub>3</sub>. *Phys. Rev. B* **99**, 104111 (2019).
25. Amelitchev, V. A. *et al.* Structural and chemical analysis of colossal magnetoresistance manganites by Raman spectrometry. *Phys. Rev. B* **63**, 104430 (2001).
26. Herrero-Martín, J., Blasco, J., García, J., Subías, G. & Mazzoli, C. Structural changes at the semiconductor-insulator phase transition in the single-layered perovskite La<sub>0.5</sub>Sr<sub>1.5</sub>MnO<sub>4</sub>. *Phys. Rev. B* **83**, 184101 (2011).
27. Stevens, T., Kuhl, J. & Merlin, R. Coherent phonon generation and the two stimulated Raman tensors. *Phys. Rev. B* **65**, 3–6 (2002).
28. Trigo, M. *et al.* Fourier-transform inelastic scattering from time- and momentum-dependent phonon – phonon correlations. *Nat. Phys.* **9**, 790–794 (2013).
29. Otto, M. R. *et al.* Mechanisms of electron-phonon coupling unraveled in momentum and time: The case of soft phonons in TiSe<sub>2</sub>. *Sci. Adv.* **7**, eabf2810 (2021).
30. René de Cotret, L. P. *et al.* Direct visualization of polaron formation in the thermoelectric SnSe. *Proc. Natl. Acad. Sci.* **119**, e2113967119 (2022).
31. Billinge, Simon. J. L. Polarons in Manganites; Now You See Them Now You Don't. in *Physics of Manganites* (eds. Kaplan, T. A. & Mahanti, S. D.) 201–210 (Springer US, Boston, MA, 2002).  
doi:10.1007/0-306-47091-8\_12.

32. Vasiliu-Doloc, L. *et al.* Charge Melting and Polaron Collapse in  $\text{La}_{1.2}\text{Sr}_{1.8}\text{Mn}_2\text{O}_7$ . *Phys. Rev. Lett.* **83**, 4393–4396 (1999).
33. Li, J. *et al.* Dichotomy in ultrafast atomic dynamics as direct evidence of polaron formation in manganites. *Npj Quantum Mater.* **1**, 16026 (2016).
34. Pfeifer, M. A., Williams, G. J., Vartanyants, I. A., Harder, R. & Robinson, I. K. Three-dimensional mapping of a deformation field inside a nanocrystal. *Nature* **442**, 63–6 (2006).
35. Thygesen, P. M. M. *et al.* Local structure study of the orbital order / disorder transition in  $\text{LaMnO}_3$ . *Phys. Rev. B* **95**, 174107 (2017).
36. Wall, S. *et al.* Ultrafast disordering of vanadium dimers in photoexcited  $\text{VO}_2$ . *Science* **362**, 572–576 (2018).
37. Johnson, A. S. *et al.* All-optical seeding of a light-induced phase transition with correlated disorder. *Nat. Phys.* 1–6 (2024) doi:10.1038/s41567-024-02474-4.
38. Johnson, A. S. *et al.* Ultrafast Loss of Lattice Coherence in the Light-Induced Structural Phase Transition of  $\text{V}_2\text{O}_3$ . *Phys. Rev. Lett.* **129**, 255701 (2022).
39. Tobey, R., Prabhakaran, D., Boothroyd, A. & Cavalleri, A. Ultrafast Electronic Phase Transition in  $\text{La}_{1/2}\text{Sr}_{3/2}\text{MnO}_4$  by Coherent Vibrational Excitation: Evidence for Nonthermal Melting of Orbital Order. *Phys. Rev. Lett.* **101**, 197404 (2008).
40. Först, M. *et al.* Nonlinear phononics as an ultrafast route to lattice control. *Nat. Phys.* **7**, 854–856 (2011).
41. Dodge, J. S., Lopez, L. & Sahota, D. G. Optical Saturation Produces Spurious Evidence for Photoinduced Superconductivity in  $\text{K}_3\text{C}_{60}$ . *Phys. Rev. Lett.* **130**, 146002 (2023).
42. Ingold, G. *et al.* Experimental station Bernina at SwissFEL: condensed matter physics on femtosecond time scales investigated by X-ray diffraction and spectroscopic methods. *J. Synchrotron Radiat.* **26**, 874–886 (2019).

43. Ishikawa, T., Ookura, K. & Tokura, Y. Optical response to orbital and charge ordering in a layered manganite:  $\text{La}_{1/2}\text{Sr}_{3/2}\text{MnO}_4$ . *Phys. Rev. B* **59**, 8367–8370 (1999).
44. Henke, B. L., Gullikson, E. M. & Davis, J. C. X-Ray Interactions: Photoabsorption, Scattering, Transmission, and Reflection at  $E = 50\text{--}30,000$  eV,  $Z = 1\text{--}92$ . *At. Data Nucl. Data Tables* **54**, 181–342 (1993).